OFFICE OF NAVAL RESEARCH
DEPARTMENT OF THE NAVY
CONTRACT N00014-67-0094-0009

COLLAPSE OF AN INITIALLY SPHERICAL VAPOR CAVITY IN THE NEIGHBORHOOD OF A SOLID BOUNDARY

BY
MILTON S. PLESSET AND RICHARD B. CHAPMAN

DIVISION OF ENGINEERING AND APPLIED SCIENCE
CALIFORNIA INSTITUTE OF TECHNOLOGY
PASADENA, CALIFORNIA

REPORT NO. 85-49 JUNE 1970

Office of Naval Research
Department of the Navy
Contract N00014-67-0094-0009

COLLAPSE OF AN INITIALLY SPHERICAL VAPOR CAVITY IN THE NEIGHBORHOOD OF A SOLID BOUNDARY

by

Milton S. Plesset and Richard B. Chapman

Division of Engineering and Applied Science
California Institute of Technology
Pasadena, California

Report No. 85-49

June 1970

Summary

Vapor bubble collapse problems lacking spherical symmetry are solved here using a numerical method designed especially for these problems. Viscosity and compressibility in the liquid are neglected. The method uses finite time steps and features an iterative technique for applying the boundary conditions at infinity directly to the liquid at a finite distance from the free surface. Two specific cases of initially spherical bubbles collapsing near a plane solid wall were simulated: a bubble initially in contact with the wall, and a bubble initially half its radius from the wall at the closest point. It is shown that the bubble develops a jet directed towards the wall rather early in the collapse history. Free surface shapes and velocities are presented at various stages in the collapse. Velocities are scaled like $(\Delta p/\rho)^{\frac{1}{2}}$ where ρ is the density of the liquid and Δp is the constant difference between the ambient liquid pressure and the pressure in the cavity. For $\frac{\Delta p}{\rho} = 10^6 \left(\frac{\text{cm}}{\text{sec}}\right)^2 \approx \frac{\text{1 atm.}}{\text{density of water}}$ the jet had a speed of about 130 m/sec in the first case and 170 m/sec in the second when it struck the opposite side of the bubble. Such jet velocities are of a magnitude which can explain cavitation damage. The jet develops so early in the bubble collapse history that compressibility effects in the liquid and the vapor are not important.

Collapse of an Initially Spherical Vapor Cavity in the Neighborhood of a Solid Boundary

Introduction

The study of the behavior of a bubble in a liquid is greatly simplified by the assumption of spherical symmetry. Following Rayleigh's (1917) classical analysis of a problem first solved by Besant, the inviscid collapse of a spherical cavity in a homogeneous, incompressible liquid under a constant ambient pressure, numerous authors have studied the behavior of spherical bubbles under a wide range of conditions. Far less is known about the nonspherical behavior of bubbles. Because problems lacking spherical symmetry have proven too complex for direct analysis, they have been investigated primarily by qualitative reasoning, experiments, and perturbations from spherically symmetric solutions.

A problem of primary importance is the interaction of a collapsing bubble with a solid surface. The earliest theory of cavitation damage was based on the high pressures developed near a spherical cavity which has collapsed to a small fraction of its initial size. A more recent theory includes the pressures developed during rebound caused by the compression of a small amount of permanent gas contained in the bubble. Calculations discussed by Plesset (1966) indicate that stresses produced by the collapse and subsequent rebound of a spherical bubble fall off rapidly as the distance from the bubble is increased and are too small to damage a solid surface unless the surface is quite close to the bubble. Thus the presence of a solid boundary will have an important effect in destroying the spherical symmetry of any bubble capable of producing damage.

Another explanation of cavitation damage is the theory, first suggested by Kornfeld and Suvorov (1944), that damage is caused by the action of liquid jets formed on bubbles near the solid surface. A perturbation study by Rattray (1951) suggested that the effect of a solid wall in disturbing the flow during the collapse of an initially spherical bubble could cause the formation of a liquid jet directed towards the wall.

Experiments by Benjamin and Ellis (1966) later confirmed that jets form on bubbles collapsing near a solid wall. Large vapor bubbles, generally about one centimeter in radius, were grown from small nuclei by the application of a negative pressure. High speed photographs were taken of these bubbles as they collapsed near a plane solid surface. The ambient pressure was maintained at about 0.04 atm during collapse so that collapse velocities would be reduced to facilitate the photography. These bubbles were nearly spherical as they started collapsing. First they became elongated in the direction normal to the wall; then they tended to flatten and form an inward moving jet on the side of the bubble opposite the wall.

The advantages of a numerical technique for simulating nonspherical bubble collapse are clear. Experiments are difficult and give only sketchy results. Perturbations from spherically symmetric solutions are not valid for large deformations. A numerical solution, however, can check results and supply detailed information. Numerical methods can also be applied to situations which might be very difficult to produce in the laboratory. Mitchell, Kling, Cheesewright, and Hammitt (1967) have considered simulation of bubble collapse using the Marker-and-Cell technique, a general method for simulating incompressible, viscid flows with an assortment of boundary conditions including free surfaces. Because nonspherical collapse is of such interest,it is worthwhile to develop a method of simulation especially suited to these problems.

Definition of the Problem

The asymmetries caused by a solid wall should be separated from those due to initial asymmetries in shape or velocity of the type analyzed in the linearized theory of Plesset and Mitchell (1956). The bubble is therefore taken to be spherical and at rest at the initiation of the collapse, and any other extraneous asymmetric effects such as gravity are also omitted.

The following assumptions will be made:

1. The liquid is incompressible.
2. The flow is nonviscous.
3. The vapor pressure is uniform throughout the bubble interior.
4. The ambient pressure and the vapor pressure are constant with time.
5. The bubble contains no permanent gas.
6. Surface tension effects are negligible.

This set of assumptions defines the problem as the nonspherical version of the classical Rayleigh collapse calculation. Only the first three assumptions are essential to the method of simulation developed here. The last three assumptions are made to keep the essential features of the problem in the foreground. With the absence of shocks, compressibility will not become important until speeds in the liquid are comparable with the speed of sound. Thus the liquid can be assumed to be incompressible with the understanding that solutions are valid for small Mach numbers only. In most cases of collapse, viscosity can be neglected unless the bubble is initially very small. For example, viscosity is unimportant for a spherical bubble collapsing in water under atmospheric pressure if the initial radius is 10^{-3} cm or greater. As for the assumption of uniform pressure inside the bubble, this assumption will remain valid as long as speeds on the bubble surface are below the speed of sound in the vapor.

The problem is specified by the following conditions:

p_∞ = ambient pressure,
p_v = vapor pressure inside the bubble,
R_o = initial radius of the bubble,
b = initial distance from the plane wall to the center of the bubble.

Because the flow is irrotational, the velocity vector $\vec{v}$ can be written in terms of a velocity potential φ. Since incompressibility is assumed, φ must satisfy Laplace's equation throughout the liquid.

The pressure boundary conditions can be restated in terms of φ and v with the aid of Bernoulli's equation

$$\frac{\partial \varphi}{\partial t} + \frac{v^2}{2} + \frac{p}{\rho} = c(t) \quad . \tag{1}$$

Infinitely far from the bubble the velocity is zero, and the pressure is the ambient pressure. The velocity potential there is an arbitrary function of time only, which can be taken to be zero:

$$\lim_{|\vec{x}| \to \infty} \varphi(\vec{x}, t) = 0 \quad . \tag{2}$$

Then on the free surface,

$$\frac{\partial \varphi}{\partial t} + \frac{v^2}{2} = \frac{p_\infty - p_v}{\rho} = \frac{\Delta p}{\rho} \quad . \tag{3}$$

The final boundary condition on the potential is that its normal derivative must vanish at the solid wall. Initially the potential is uniformly zero.

As a result of the assumptions, the solutions are characterized by the single parameter b/R_o. A solution for a particular value of b/R_o can be scaled to bubbles of any initial size under any positive collapsing pressure Δp. Velocities are independent of the size of the bubble, and are scaled like $(\Delta p/\rho)^{\frac{1}{2}}$.

The Method of Simulation

Clearly the irrotationality of these problems is best exploited by solving them in terms of the velocity potential. A single variable gives a great simplification to almost every aspect of the calculation. If desired, both the velocity and the pressure can be easily calculated from the solution in terms of the potential.

The numerical method should also reflect the fact that the interest in these problems is centered on the flow at and near the bubble free surface. The method used here calculates the velocity only on the bubble surface. The potential should vary most rapidly near the bubble and quite slowly far from the bubble. Thus, it is necessary to have a highly accurate and detailed solution near the bubble surface. For a finite difference method this requirement means that the grid should be finest

near the free surface. The procedure adopted here used a series of progressively finer nets.

Modified finite difference equations at an irregular boundary, usually referred to as irregular stars, are essential for an accurate solution near the boundary. In their numerical study of finite-amplitude water waves Chan, Street, and Strelkoff (1969) observed that the wave-forms became unstable after a few cycles using the Marker-and-Cell method. They obtained satisfactory results, however, with their SUMMAC method, a modified MAC technique using irregular stars at the free surface.

A basic question in the numerical simulation of axially symmetric bubble collapse is whether to base the finite difference scheme on spherical coordinates or on cylindrical coordinates. The location of the origin of the spherical system also can present a problem, especially if the bubble is highly deformed. Because of the singularity, the origin cannot be placed in or adjacent to the liquid. Another disadvantage of spherical coordinates is that the boundary condition at the wall cannot be easily imposed. In a finite difference method based on cylindrical coordinates, the boundary condition at the solid wall is simple and straightforward to apply. For these reasons a finite difference scheme based on cylindrical coordinates was adopted. A spherical coordinate system, however,with the origin on the solid wall was used in applying the condition at infinity to the outer boundary.

The problems considered are axially symmetric so that the bubble and the liquid surrounding it can be described in any half plane bounded by the axis of symmetry. These problems also contain a plane solid wall so that they can be further reduced to a single quadrant.

The method of flow simulation is based on a series of small time steps. The shape and the potential distribution of the free surface forming the bubble is known at the beginning of each time step. The boundary condition at the free surface combined with the condition at infinity and the boundary conditions on the solid wall and on the axis of symmetry determine the potential throughout the liquid. The velocities of points on the

free surface can then be calculated. If the time step Δt is small enough, the velocities will remain relatively constant throughout the time step. Then the displacement of a point on the free surface with velocity $\vec{v}$ is approximately

$$\vec{\Delta x} = \vec{v}\Delta t \quad . \tag{4}$$

Bernoulli's equation is used to get the rate of change of the potential of a point moving with the free surface,

$$\frac{D\varphi}{Dt} = \frac{\partial \varphi}{\partial t} + \vec{v}\cdot\vec{\nabla}\varphi = \frac{\partial \varphi}{\partial t} + v^2 \quad , \tag{5}$$

in the form

$$\frac{D\varphi}{Dt} = \Delta p/\rho + \frac{1}{2} v^2 \quad . \tag{6}$$

For Δt small, the change in the potential of a displaced point on the free surface is approximately

$$\Delta\varphi = \left[\Delta p/\rho + \frac{1}{2} v^2\right]\Delta t \quad . \tag{7}$$

The velocities are, of course, computed at the beginning of the time step. After the free boundary has been displaced and the potentials on it changed accordingly, the new bubble shape with the new potential distribution on the free surface can be used for another time step.

Standard finite difference approximations similar to Shaw's (1953) are used to represent Laplace's equation in cylindrical coordinates (r, z). The domain of interest in the (r, z)-plane is covered with a square grid, or net, formed by a family of horizontal (z = constant) net lines parallel to the solid wall and a family of vertical (r = constant) net lines parallel to the axis of symmetry. Lines of both families are separated by a constant distance h called the mesh length. The potential distribution throughout the liquid is described by the potentials of points, called nodal points, where the two families of net lines intersect. The free

boundary is represented in the calculation by the set of points where the free surface and the net lines intersect (cf. Fig. 1).

A typical nodal point and its four neighboring nodal points, each a distance h from the central point, form a regular star. If a star is centered in the liquid but is near the free surface, some of its outer nodal points may fall inside the bubble. Such stars are called irregular stars because the nodal point inside the bubble must be replaced by a free surface point of known potential creating a leg shorter than the mesh length h. Stars centered inside the bubble are not used in the calculations. The positions of points in both regular and irregular stars with respect to the central or "0" point are identified by the numbering system illustrated in Fig. 2.

The finite difference equation at a star is derived by expanding the potential about the central point and neglecting the higher derivatives (see Shaw, for example). The equation for regular stars off the axis is

$$\varphi_o = \frac{1}{4}\left[\varphi_4 + \varphi_2 + \varphi_1\left(1 + \frac{h}{2r_o}\right) + \varphi_3\left(1 - \frac{h}{2r_o}\right)\right] . \qquad (8)$$

Stars centered on the axis of symmetry need special consideration because of the $\frac{1}{r}\varphi_r$ term in the Laplacian. In this case φ is expanded for constant z in powers of r about the axis of symmetry,

$$\varphi = a + br^2 + \ldots \quad (r \text{ small}, \ z \text{ constant}) . \qquad (9)$$

A linear term cannot be present in the expansion since it would imply a line source of fluid on the axis. For a regular star centered on the axis of symmetry

$$\lim_{r\to 0}\left(\varphi_{rr} + \frac{1}{r}\varphi_r\right) = 4b \approx 4(\varphi_1 - \varphi_o)h^{-2} . \qquad (10)$$

The resulting finite difference approximation is

$$\varphi_o = \frac{1}{6}\left[\varphi_2 + \varphi_4 + 4\varphi_1\right] . \qquad (11)$$

Stars centered directly adjacent to the axis of symmetry at $r = h$ must be considered. The equation for these stars is also derived from an expansion about the axis of symmetry for constant z. The resulting equation for regular stars at $r = h$ is

$$\varphi_o = \frac{1}{2} (\varphi_2 + \varphi_4 + \varphi_1 - \varphi_3) \quad . \tag{12}$$

Since the solid wall forms a plane of symmetry, stars centered on the wall must satisfy the relation

$$\varphi_2 = \varphi_4 \quad . \tag{13}$$

This condition is imposed simply by using the appropriate star equation with φ_2 substituted for φ_4.

The boundary condition at the free surface enters the calculation through the irregular stars. Equations for these stars contain the sizes of the irregular legs as parameters but are derived in the same way as the corresponding regular star equations.

Each star equation can be written as a formula for the potential of the central point of the star in terms of the central potentials of neighboring stars. The Liebmann iterative method is used with over-relaxation to find the potential distribution that solves all star equations simultaneously. Each iteration of the Liebmann method covers every star in the net. The central potential at each star is, in turn, replaced with a new value based on the star equation. The Liebmann method employs this new potential in the equations of any neighboring stars that are encountered later in the iteration in contrast with another common method, the Richardson method, which does not use the new potentials until an iteration has been completed. An initial estimate of the potential distribution is necessary to start the Liebmann method. Usually this is provided by the potential distribution from the preceeding time step. The first time steps and time steps immediately following a change in the nets are initiated from a uniformly zero potential.

The convergence of the Liebmann method for large nets is greatly

accelerated by the use of overrelaxation. Suppose φ_s is the potential, of the central point that satisfies the star equation. Then the old potential φ_{old}, is replaced by

$$\varphi_{new} = \varphi_{old} + \alpha(\varphi_s - \varphi_{old}) \quad , \qquad 1 \leqslant \alpha < 2 \quad . \tag{14}$$

The constant α is called the relaxation factor. A simple estimate of the optimum relaxation factor and the rate of convergence for large nets was developed for the plane case by P. R. Garabedian (1956). His results are formally unchanged in the axially symmetric case. After N iterations the error is reduced by a factor of the order of magnitude

$$E = O(e^{-qNh}) \tag{15}$$

where q is defined by

$$q = \mathrm{Re}\{2C - (4C^2 - 2k_1^2)^{\frac{1}{2}}\} \quad . \tag{16}$$

The constant C is related to the relaxation factor by

$$\alpha = \frac{2}{1 + Ch} \quad , \tag{17}$$

and k_1 is the lowest eigenvalue of the problem

$$\nabla^2 U + k_n^2 U = 0 \quad . \tag{18}$$

The boundary conditions on U are the same as on the error in the potential: U is zero on boundaries of known potential and has a zero, normal derivative on boundaries where the normal derivative is known.

Clearly convergence is most rapid when q is maximized. Garabedian pointed out that,if C is made greater than $k_1/\sqrt{2}$, the real part of $-(4C^2 - 2k_1^2)^{\frac{1}{2}}$ will decrease sharply, reducing convergence considerably; but,if C is less than or equal to the optimum $k_1/\sqrt{2}$, then

$-(4C^2 - 2k_1^2)^{\frac{1}{2}}$ is purely imaginary so that

$$q = 2\,\frac{(2-\alpha)}{\alpha h} \quad . \tag{19}$$

If we assume that α is large enough to cover the lowest eigenvalue, i.e.,

$$\alpha \geqslant \frac{2}{1+k_1 h/\sqrt{2}} \quad , \tag{20}$$

then the rate of convergence is a function of α only,

$$E = O\left(\exp -N\left(\frac{4-2\alpha}{\alpha}\right)\right) \quad . \tag{21}$$

In many problems, the optimum value of α can be estimated quite closely. A useful example is that of two concentric spheres with known potential distributions on their surfaces. Let J be the number of mesh lengths between the two spheres. The optimum relaxation factor is then

$$\alpha = \frac{2}{1+\pi/(\sqrt{2}\,J)} \quad , \tag{22}$$

which corresponds to an error reduction factor of

$$E = O\left(\exp - N\left(\frac{\sqrt{2}\,\pi}{J}\right)\right) \quad . \tag{23}$$

An iterative method has been developed for applying the condition at infinity to the outer boundary. The outer boundary refers to the boundary of the net excluding the free boundary, the axis of symmetry, and the solid wall. The method is based on a spherical coordinate system (d, θ) with its origin at the intersection of the axis of symmetry and the solid wall. The distance from the origin is d; the angle with the axis of symmetry is θ. Each step begins with a net like the one shown in Fig. 3. The shape of this net is chosen to give the nodal points on the outer boundary a nearly constant value of d. A slight point to point variation in d is unimportant, however. Irregular stars are unnecessary on the outer boundary. The average value of d on the outer boundary is taken

to be d_o.

The potential can be expanded in a series of axially symmetric harmonics valid for values of d large enough to contain the bubble completely

$$\varphi(d,\theta) = \sum_{k=o}^{\infty} (A_{2k} d^{2k} + B_{2k} d^{-(2k+1)}) P_{2k}(\cos\theta) \quad . \qquad (24)$$

Only the even Legendre polynomials are used in the expansion because of the symmetry of the plane wall. The condition that the potential approaches zero infinitely far from the bubble may be restated as

$$A_{2n} = 0 \quad , \quad n = 1,2,3 \ . \ . \ . \quad . \qquad (25)$$

The A coefficients will be zero only when the potential distribution on the outer boundary is consistent with the condition at infinity. It is assumed that d_o is large enough so that the terms in $P_o(\cos\theta)$ and $P_2(\cos\theta)$ effectively describe the potential on the outer boundary. The $P_4(\cos\theta)$ term is also included in the calculation, although d_o is large enough in practice to keep this term negligible. The potential at the outer boundary may then be written as

$$\varphi(d_o,\theta) = \left(A_o + \frac{B_o}{d_o}\right) + \left(A_2 d_o^2 + \frac{B_2}{d_o^3}\right) P_2(\cos\theta) + \left(A_4 d_o^4 + \frac{B_4}{d_o^5}\right) P_4(\cos\theta) \quad ,$$

$$= C_o + C_2 P_2(\cos\theta) + C_4 P_4(\cos\theta) \quad . \qquad (26)$$

Each time step begins by solving the potential problem with a trial potential distribution on the outer boundary. This potential distribution is usually provided by the results of the previous time step. The condition that the A coefficients must vanish may be stated as a relationship between the potential and its radial derivative. Therefore, the radial derivative is calculated at each nodal point on the outer boundary. All nodal points on the outer boundary of nets like the one in Fig. 3 have other nodal points directly below them and to their left. The derivative

in the vertical direction can be calculated by fitting a second order polynomial through the outer boundary nodal point and the two nodal points directly below it. The horizontal derivative is calculated by the same method and combined with the vertical derivative to produce the radial derivative:

$$\frac{\partial \varphi}{\partial d}(d_o, \theta) = \left(\frac{\partial \varphi}{\partial z}\right)_r \cos\theta + \left(\frac{\partial \varphi}{\partial r}\right)_z \sin\theta$$

$$= -\frac{B_o}{d_o^2} + \left(2A_2 d_o - 3\frac{B_2}{d_o^4}\right) P_2(\cos\theta)$$

$$+ \left(4A_4 d_o^3 - 5\frac{B_4}{d_o^6}\right) P_4(\cos\theta) \quad ,$$

$$\equiv D_o + D_2 P_2(\cos\theta) + D_4 P_4(\cos\theta) \quad . \tag{27}$$

The C and D coefficients are easily evaluated from the potential on the outer boundary and its radial derivative. The A and B coefficients are determined by the C and D coefficients. In particular,

$$B_o = -D_o d_o^2 \tag{28a}$$

$$B_2 = (2C_2 d_o^3 - D_2 d_o^4)/5 \quad , \tag{28b}$$

and

$$B_4 = (4C_4 d_o^5 - D_4 d_o^6)/9 \tag{28c}$$

The condition that the A coefficients vanish can be stated as a relationship between the C and B coefficients:

$$C_{2k} = B_{2k} d_o^{-(2k+1)} \quad . \tag{29}$$

With the neglect of the higher harmonics, Eq. (29) will be satisfied only when the potentials on the outer boundary are consistent with the condition at infinity. This suggests that the B coefficients calculated from Eqs. (28) may be used to form new potentials at the outer boundary nodal points from the formula

$$\varphi(d,\theta) = \frac{B_o}{d} + \frac{B_2}{d^3} P_2(\cos\theta) + \frac{B_4}{d^5} P_4(\cos\theta) \quad . \tag{30}$$

The iteration scheme is to solve the potential problem with the new outer boundary potentials, then find the B coefficients from Eqs. (28) and use them to establish outer boundary potentials for the next iteration. Let a superscript n on a coefficient denote the value of that coefficient during the n'th iteration. Equation (30) specifies that

$$C_{2k}^{n+1} = B_{2k}^{n} d_o^{-(2k+1)} \quad . \tag{31}$$

Convergence is rapid when the distance from the bubble to the outer wall is large compared to the mean radius of the bubble. In practice three or four iterations were sufficient to establish a satisfactory potential distribution on the outer boundary starting from a uniformly zero distribution, and only a single iteration was necessary to adjust for the small changes between consecutive time steps. The net used to establish the outer boundary potentials had a radius of 40 mesh lengths. The bubble had an initial radius of 5 mesh lengths in this net. As the bubble collapsed, the scale of this net was halved several times. The large mesh length of the net used to establish the outer boundary potentials gives only a rough solution near the free boundary. Therefore three or four progressively finer nets are applied successively to provide a more detailed description near the bubble. A typical series of nets is illustrated in Fig. 4. Each net of the series has a mesh length half the mesh length of the preceeding net. Since each net is contained in the preceeding one, both the initial potentials and the outer boundary potentials are taken from the preceeding net. The shapes of all nets except the one used to establish the outer boundary potentials are arbitrary. Usually these nets were shaped to give a minimum distance of ten to twenty mesh lengths between the free surface and the outer boundary.

The relaxation factor for the first net of the series was estimated from the model of a sphere of radius d_o with a point of known potential (representing the free boundary) at its center. The optimum relaxation factor for $J = 40$ is $\alpha = 1.895$. Then 40 Liebmann iterations reduce

the error by a factor of about 85.

The finer nets contain errors of predominantly small wavelengths. For these nets a relaxation factor capable of handling errors extending a distance of 20 meshlengths from a spherical boundary should be adequate. When $J = 20$, $\alpha = 1.80$. Since the initial errors in the finer nets are small in magnitude, 15 iterations giving an error reduction factor of about 30 should be sufficient for the intermediate nets. More iterations are advisable for the final net of the series because the velocities at the free surface points are calculated from its solution. A choice of 25 iterations gives an error reduction factor of about 250.

The velocity components in both the r and z directions must be found at all free boundary points of the final net. The velocity calculation will be described for a point on a vertical net line. The method is completely analogous for points on horizontal net lines. If the mesh length of the final net is sufficiently small, each free boundary point not centered on the wall or on the axis of symmetry will be part of an irregular star with a regular point opposite the free boundary point as in Fig. 5. Let φ_B, φ_o, and φ_D be the potentials of the free boundary point, the central point of the irregular star, and the point opposite the free boundary point, respectively. The potential along the vertical net line is approximated near the free boundary point by a quadratic fitted through points B, O, and D. The vertical velocity is then

$$\left(\frac{\partial\varphi}{\partial z}\right)_B = \frac{\mathrm{sgn}(z_D - z_B)}{h}\left[\frac{\lambda+1}{\lambda}(\varphi_o - \varphi_B) - \frac{\lambda}{\lambda+1}(\varphi_D - \varphi_B)\right]$$

where

$$\lambda = \frac{z_o - z_B}{z_D - z_o} = \frac{|z_o - z_B|}{h} = \frac{\text{length of irregular leg}}{\text{length of regular leg}} \quad . \tag{33}$$

When λ is smaller than some minimum value λ_{min}, point D is used in place of point O, and the next point along the net line (point E in Fig. 5) replaces point D. This adds unity to λ.

Once the derivative in the vertical direction has been found, the

derivative in the horizontal direction is calculated from the two free boundary points A and C on either side of point B. A linear approximation is used for the potential between adjacent free surface points. Expansion of the potential about point B along the free surface gives to first order the form

$$\varphi_A \approx \varphi_B + \left(\frac{\partial\varphi}{\partial z}\right)_B (z_A - z_B) + \left(\frac{\partial\varphi}{\partial r}\right)_B (r_A - r_B) \quad . \tag{34}$$

This produces an estimate for the horizontal velocity

$$\left(\frac{\partial\varphi}{\partial r}\right)_B \approx \frac{\varphi_A - \varphi_B - \left(\frac{\partial\varphi}{\partial z}\right)_B (z_A - z_B)}{(r_A - r_B)} \quad . \tag{35}$$

To avoid any systematic errors, this estimate is averaged with another estimate of $\left(\frac{\partial\varphi}{\partial r}\right)_B$ made using the free surface point C on the other side of B.

Since the method for finding the horizontal velocity is essentially to subtract the known vertical component from the velocity tangential to the free surface, free surface points on vertical net lines should not be used to define the displaced free surface if the tangent to the free surface at that point is nearly vertical. It is also wise to eliminate one of a pair of adjacent free surface points that are within a few hundredths of a mesh length of each other since there is a possibility that their paths may cross when they are displaced. After the free boundary points of the final net are displaced and have had their potentials changed, they are used with the proper scaling to define the free boundary in all of the nets of the next time step. To obtain the points where the free surface intersects the net lines, consecutive pairs of displaced points are connected by straight lines as illustrated in Fig. 6. A free boundary point is established wherever one of these lines intersects a net line. Its potential is determined by linear interpolation between the endpoints.

Equations (4) and (7) are accurate only if the velocities are relatively constant between consecutive time steps. The criterion to be used in choosing the size of a time step should be that the velocities of

the free boundary points must change by less than a given percentage between consecutive time steps. This is clearly impossible for the first time step if the velocities are initially zero. However, Eqs. (4) and (7) can be modified to allow a large initial step. Consider a bubble completely at rest at $t = 0$. Early in the collapse all velocities will be small. At a point on the free surface

$$\frac{D\varphi}{Dt} = \Delta p/\rho + O(v^2) \quad , \tag{36}$$

or over the free surface

$$\varphi \approx t(\Delta p/\rho) \quad . \tag{37}$$

The initial step is made by solving the potential problem with a potential of $\Delta p/\rho$ over the initial free surface and calculating the resulting velocity $\vec{V}$ at the free boundary points. Then early in the collapse

$$\vec{v} \approx t\vec{V} \tag{38}$$

After an initial time step Δt_o, the displacement and potential of a point on the free surface are

$$\Delta\vec{x} = \int_o^{\Delta t_o} \vec{v}\, dt = \frac{1}{2}\,(\Delta t_o)^2\,\vec{V} \tag{39}$$

and

$$\varphi = \int_o^{\Delta t} \left[\Delta p/\rho + \frac{1}{2}\,v^2\right] dt = (\Delta p/\rho)\Delta t_o + \frac{1}{6}\,(\Delta t_o V)^2 \Delta t_o \quad . \tag{40}$$

Results of the Calculations

The collapse of an initially spherical bubble near a plane solid wall was simulated for two cases. In Case 1 the parameter b/R_o was unity; that is, the bubble boundary was in contact with the solid wall and tangent to it. In Case 2 b/R_o was 1.5; the closest distance from the

bubble boundary to the solid wall was initially half the radius of the bubble. Ninety-four time steps were used for Case 1 and seventy-seven for Case 2. Calculations were stopped when the liquid jet reached the opposite wall of the bubble since the assumption of incompressibility is no longer valid. The bubble shapes for selected time steps for Cases 1 and 2 are shown superimposed in Figs.7 and 8, respectively. Table I lists the time intervals in units of $R_o(\rho/\Delta p)^{\frac{1}{2}}$ from the initiation of collapse for each shape and the downward velocity on the upper portion of the bubble at the axis of symmetry. The velocities, which are scaled like $(\Delta p/\rho)^{\frac{1}{2}}$, are given in meters/sec for the special value

$$\frac{\Delta p}{\rho} = \frac{10^6 \text{ dynes/cm}^2}{1.0 \text{ g/cm}^3} \approx \frac{1 \text{ atm.}}{\text{density of water}} \quad . \qquad (41)$$

TABLE I

Time Interval from Initiation of Collapse, and the Velocity of the Bubble Boundary at the Axial Point most Distant from the Wall, for the Cases Illustrated in Fig. 7 and Fig. 8

	Figure 7		Figure 8	
Shape	Time	Velocity	Time	Velocity
A	0.63	7.7 m/sec	0.725	10 m/sec
B	0.885	19 m/sec	0.875	17 m/sec
C	0.986	42 m/sec	0.961	35 m/sec
D	1.013	65 m/sec	0.991	53 m/sec
E	1.033	100 m/sec	1.016	94 m/sec
F	1.048	125 m/sec	1.028	142 m/sec
G	1.066	129 m/sec	1.036	160 m/sec
H	1.082	129 m/sec	1.044	165 m/sec
I	1.098	128 m/sec	1.050	170 m/sec
J	1.119	128 m/sec		

The solid wall influences the bubble early in the collapse chiefly by reducing the upward motion of the lower portion of the bubble. As a result the bubble becomes elongated in the direction normal to the wall as was predicted by Rattray (1951). The bottom of the bubble still moves upward towards the bubble center in Case 2, but since this upward motion is reduced, the centroid of the bubble moves towards the wall displaying the well-known Bjerknes effect.

As the bubble acquires kinetic energy, this energy is concentrated in the upper portion of the bubble which eventually flattens and forms a jet. Once the jet is formed, the speed of its tip remains fairly constant.

The behavior of the upper portion of the bubble in Case 2 is not very different from Case 1. The overall shapes appear quite different, however, because the bottom of the bubble must remain in contact with the solid wall in Case 1 but is allowed mobility in Case 2. The jet speed in Case 2 (about 170 m/sec under atmospheric Δp) is somewhat larger than the speed in Case 1 (about 130 m/sec). This behavior is as expected since a bubble which is farther from the wall collapses to a smaller size and can concentrate its energy over a smaller volume.

The jet appears to be the result of the deformation caused by the presence of the wall during the early part of the collapse. It is known from the linearized theory of Plesset and Mitchell (1956) that a small deformation can lead to jetting much later in the collapse, but the jet formation found here appears before the jetting which might develop from a small initial perturbation.

Although the bubble is initially fairly close to the wall in Case 2, the final jet must pass through the liquid for a distance of more than five times its diameter before it reaches the solid wall. The jet in Case 1, which strikes the wall directly, seems the more capable of damage even though the jet speed is lower. Apparently cavitation bubbles must almost touch the wall initially to be capable of damaging it.

A jet of speed v directly striking a solid boundary produces an initial pressure given by the water hammer equation,

$$p_{WH} = \rho_L c_L v \left(\frac{\rho_s c_s}{\rho_L c_L + \rho_s c_s} \right) \tag{42}$$

where the L and s subscripts refer to the liquid and the solid, respectively, Usually $\rho_s c_s$ is large compared to $\rho_L c_L$ producing the approximation

$$p_{WH} \approx \rho_L c_L v \quad . \tag{43}$$

Experiments by Hancox and Brunton (1966) have shown that multiple impacts by water at a speed of 90 m/sec can erode even stainless steel.

Benjamin and Ellis (1966) present two series of photographs of bubbles collapsing near a solid wall in Figs. 3 and 4 of their paper. The collapse illustrated in their Fig. 4 is very similar to Case 2. The collapse illustrated in their Fig. 3 falls between Case 1 and Case 2. Benjamin and Ellis estimated the jet speed in their Fig. 3 to be about 10 m/sec under an ambient pressure of about 0.04 atm. The vapor pressure of the water is very important at this reduced pressure. Since Benjamin and Ellis did not mention the temperature of the water, this pressure cannot be determined directly. However, Δp can be deduced from the total collapse time which they gave as 10 millisec. The total collapse time for a spherical bubble is, according to Rayleigh,

$$\tau = 0.915 R_o (\rho / \Delta p)^{\frac{1}{2}} \quad . \tag{44}$$

The total collapse times for Cases 1 and 2 are only slightly greater since most of the time is consumed early in the collapse while the bubble is nearly spherical. For collapse near a solid wall, then, the total collapse

time is roughly*

$$\tau \approx R_o(\rho/\Delta p)^{\frac{1}{2}} \quad . \tag{45}$$

Since $R_o \approx 1.0$ cm and $\tau = 10$ ms, the pressure difference for the collapse in Fig. 3 of Benjamin and Ellis is approximately

$$\Delta p = p_\infty - p_v \approx 10^4 \text{ dynes/cm}^2 \approx 0.01 \text{ atm} \quad . \tag{46}$$

A vapor pressure of 0.03 atm. corresponds to a temperature of about 76°F. Speeds for one atmosphere pressure difference should be increased by a factor of ten giving an estimated jet speed of roughly 100 m/sec so that the experimental observation of Benjamin and Ellis are compatible with the calculations performed here.

As general conclusions we may say that it appears very likely that cavitation damage with collapsing vapor bubbles is caused by the impact of the jet produced by the presence of the adjacent solid wall. Further, it appears reasonable to say that only those cavitation bubbles quite near the solid boundary can produce damage whether by a jet or by any radiated shock. From the calculations presented here, we see that for a bubble near the wall the jet is formed early in the collapse history so that the many complications of the late stages of cavity collapse do not enter. These familiar complications include the instability of the spherical shape toward the end of collapse, the effects of high bubble wall velocities on the behavior of the vapor in the bubble, and the effects of compressibility, not only in the vapor phase, but in the liquid as well. It is also very evident that the jet appears before there is any possibility of radiating a shock.

It is not clear that the impact, or "water-hammer" stress of Eq. (43) is the mechanism of damage to the solid. For the case of the

*Rattray derived the formula $\frac{\tau}{R_o}\left(\frac{\Delta p}{\rho}\right)^{\frac{1}{2}} = .915\left(1 + 0.41\ \frac{R_o}{2b}\right) + O\left(\frac{R_o}{2b}\right)^2$ from his perturbation analysis.

spherical bubble initially in contact with the wall and for $\Delta p = 1$ atm in water, we have $v \sim 130$ m/sec and $c_L \sim 1,500$ m/sec so that

$$p_{WH} \sim 2,000 \text{ atm.}$$

While this is a most impressive impact stress, it is not obvious that it is the important damaging mechanism since the duration of this stress is so short. We may estimate this duration as being no longer than the time for the impact signal to traverse the radius of the jet. For a bubble with an initial radius $R_o = 0.1$ cm, this time is $\tau_{WH} \sim 10^{-7}$ sec. On the other hand the stagnation pressure is approximately

$$p_s \sim \frac{1}{2} \rho v^2 \sim 800 \text{ atm}$$

which will have a duration of the order of the length of the jet divided by its velocity v. This pressure pulse may be the source of the damage because its duration is an order of magnitude greater.

Finally, we may say that cavitation damage should have a close relationship with liquid impact damage and inferences from studies of the latter should be useful for cavitation damage. We may also use calculations of the kind presented here to get reasonably accurate estimates of cavitation stress pulses.

References

Benjamin, T.B. and Ellis, A.T. 1966 Phil. Trans. Roy. Soc. London A 260, 221.

Chan R., Street, R., and Strelkoff 1969 Dept. of Civil Eng., Stanford Univ. Report 104.

Garabedian, P.R. 1956 Mathematical Tables and Other Aids to Computation X, 183.

Hancox, N.L. and Brunton, J. H. 1966 Phil Trans. Roy. Soc. London A 260, 121.

Kornfeld, M. and Suvorov, L. 1944 J. Appl. Phys. 15, 495.

Mitchell, T. M., Kling, C. L., Cheesewright, R. and Hammitt, F.G. 1967 U. of Michigan, College of Eng. Report 07738-5-T.

Plesset, M.S. 1966 Phil. Trans. Roy. Soc. London A 260, 241.

Plesset, M.S. and Mitchell, T. P. 1956 Quart. Appl. Math. 13.

Rattray, M. 1951 Ph.D. thesis, California Institute of Technology.

Rayleigh, J.W.S. 1917 Phil. Mag. 34, 94.

Shaw, F.S. 1953 An Introduction to Relaxation Methods. New York: Dover.

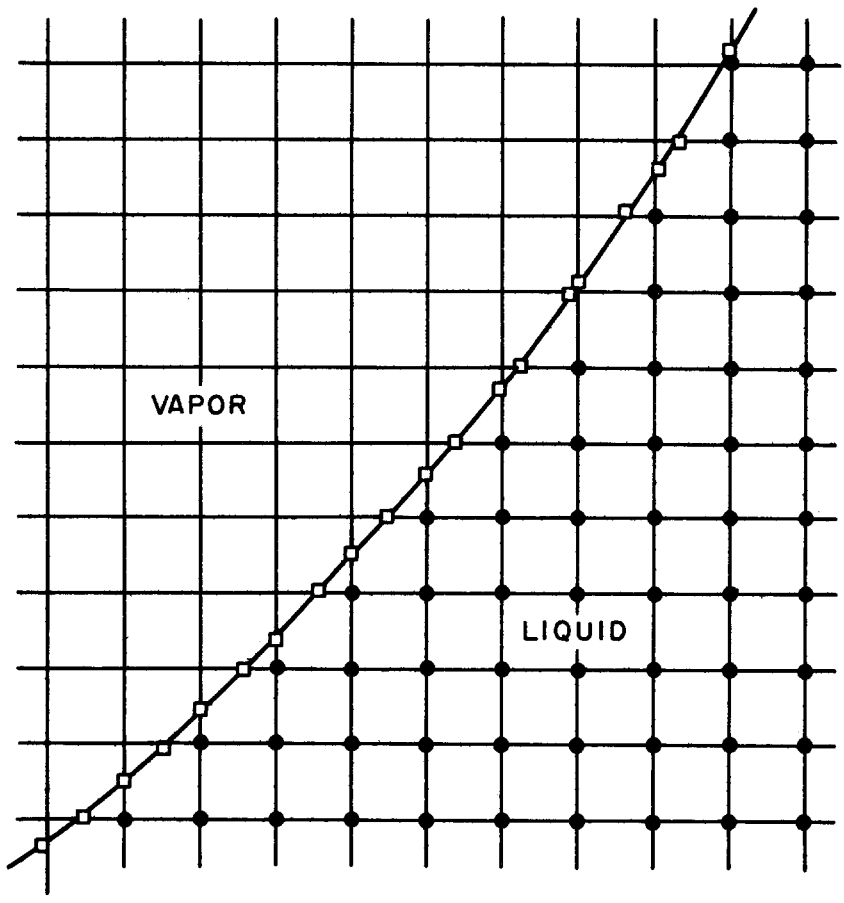

Fig. 1 Representation of the Bubble
by Free Boundary Points

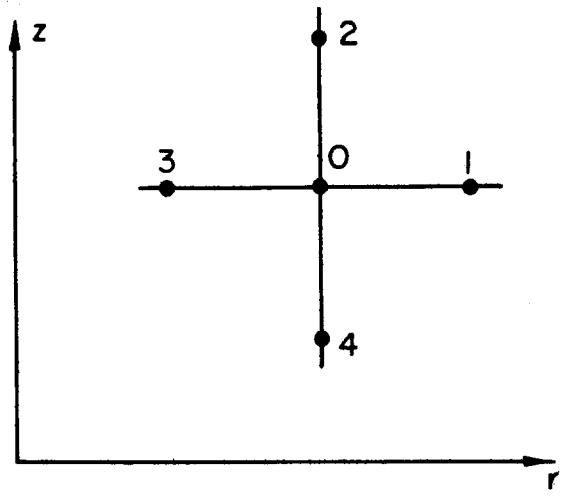

Fig. 2 Numbering System for Stars

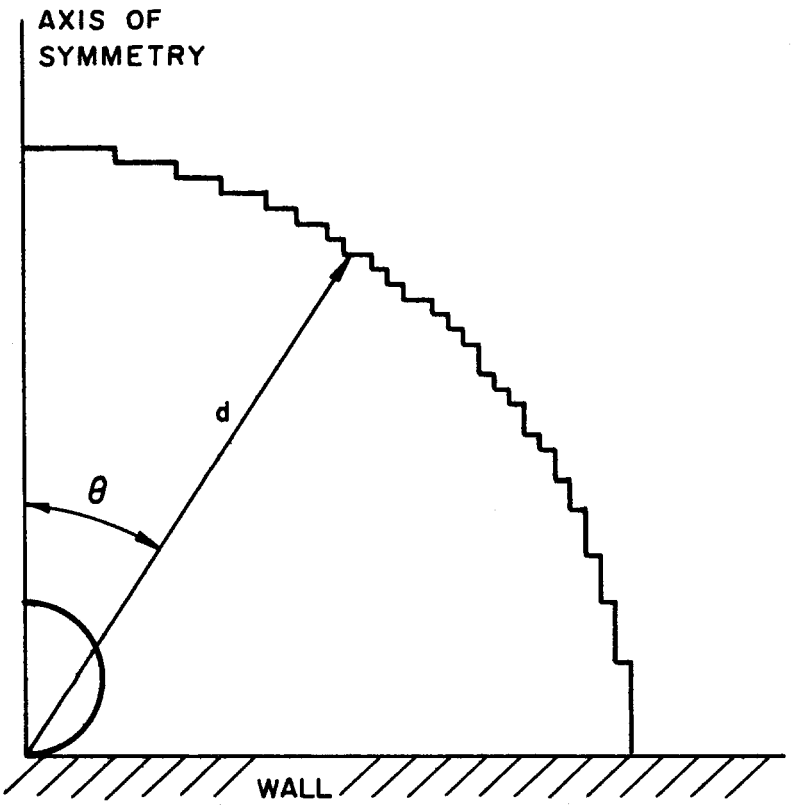

Fig. 3 Net Used to Apply the Condition at Infinity

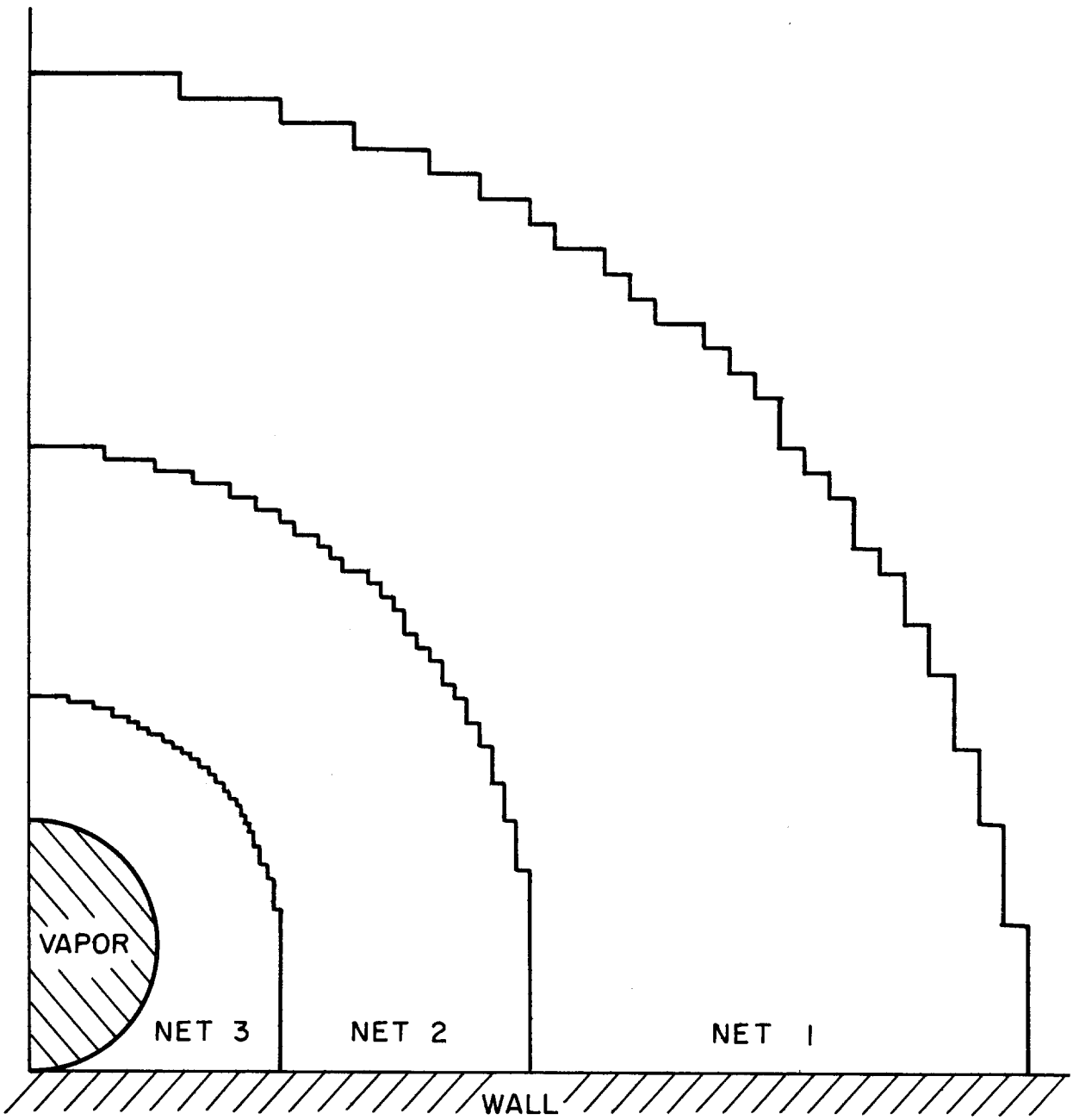

Fig. 4 A Typical Series of Nets
(Each Net Extends to the Bubble Surface)

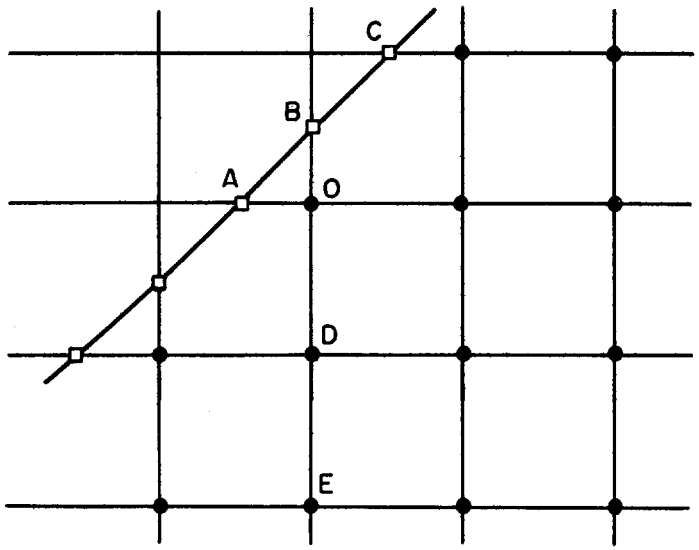

Fig. 5 Points Used to Calculate the Velocity at Free Boundary - - Point B

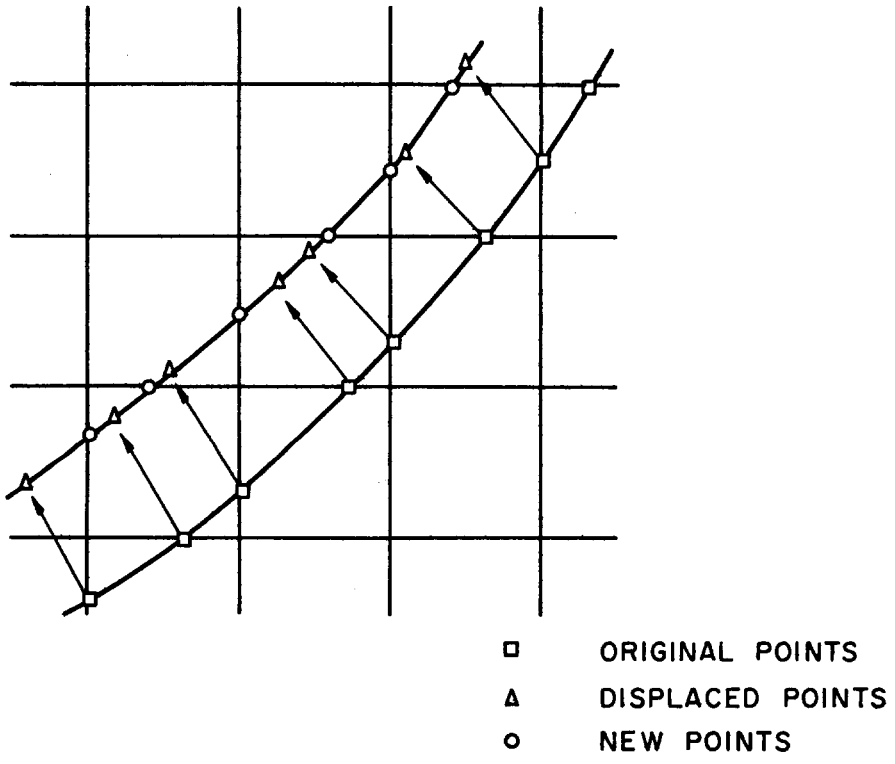

Fig. 6 Linear Interpolation to Obtain New Boundary Points

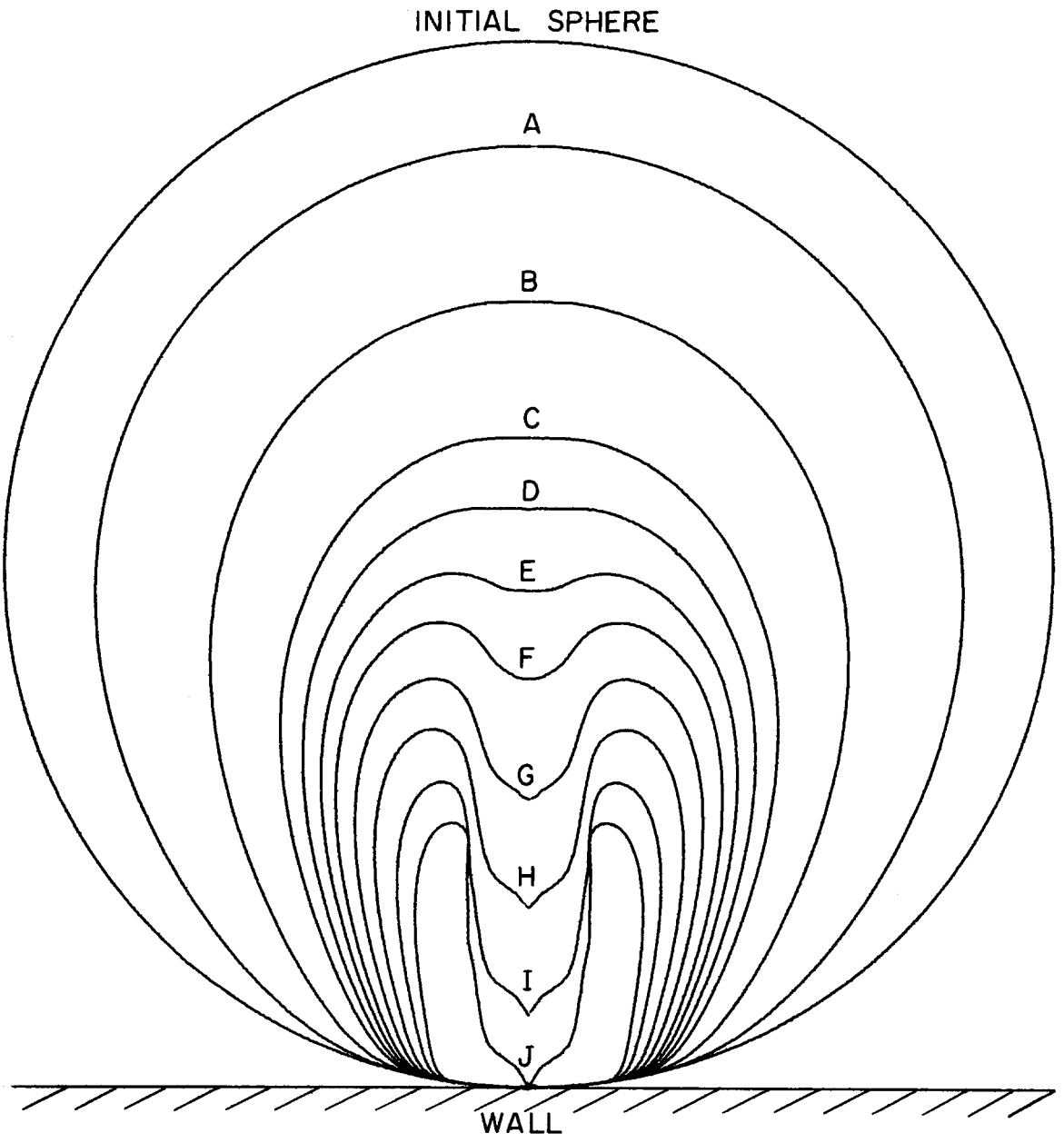

Fig. 7 Bubble Surfaces from Case 1

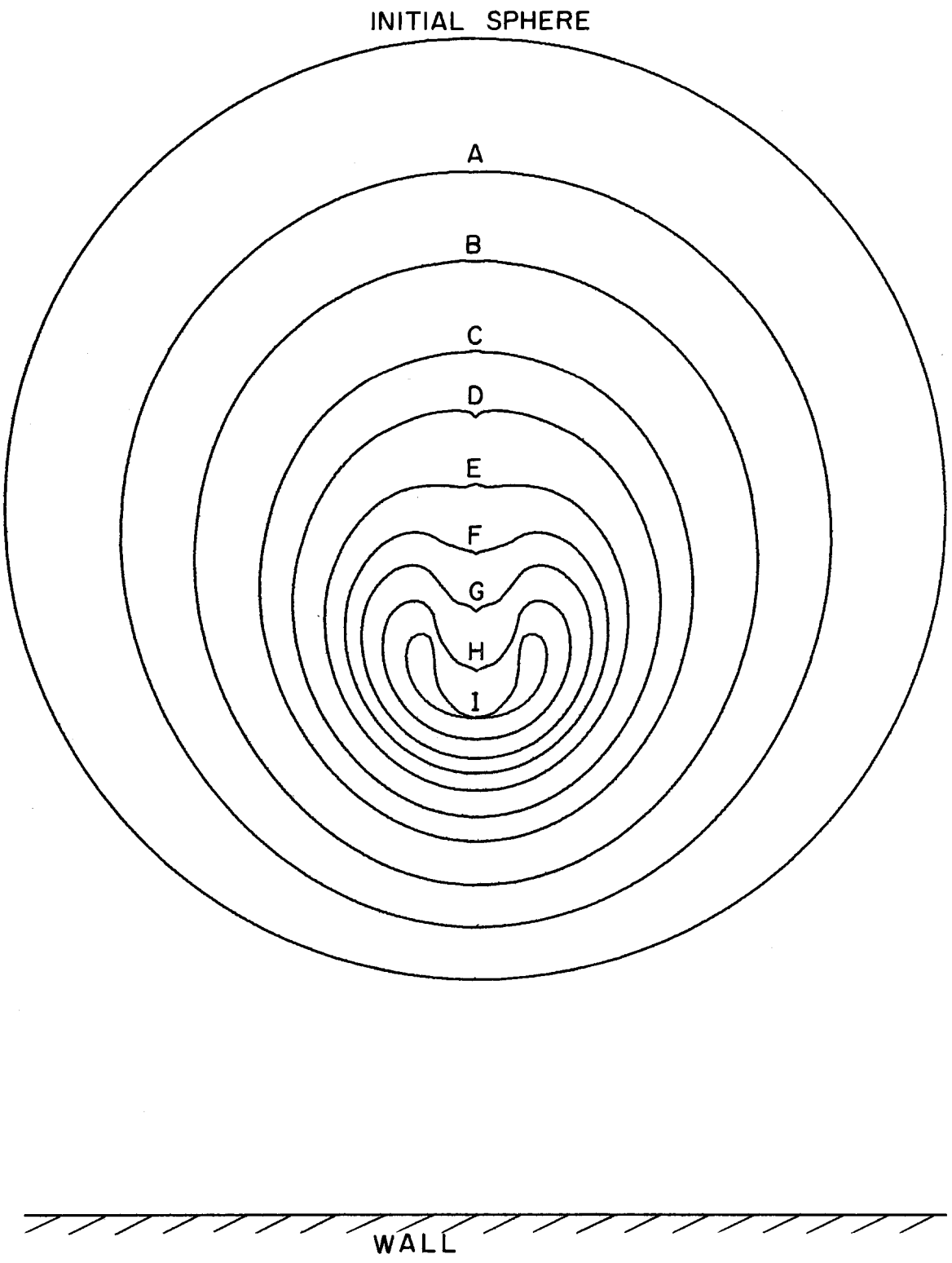

Fig. 8 Bubble Surfaces from Case 2

DISTRIBUTION LIST FOR UNCLASSIFIED TECHNICAL REPORTS

ISSUED UNDER

CONTRACT N00014-67-0094-0009

(Single copy unless otherwise specified)

Officer in Charge
Annapolis Division
Naval Ship Research & Development Center
Annapolis, Maryland 21402

Commander
Boston Naval, Shipyard
Boston, Mass. 02129

Commanding Officer
Office of Naval Research Branch Office
495 Summer Street
Boston, Mass. 02210

Commanding Officer & Director
Naval Applied Science Lab.
Naval Base, Attn: Code 930
Brooklyn, New York 11252

Naval Applied Sci. Lab.
Technical Library
Building 1, Code 222
Flushing & Washington Aves.
Brooklyn, N. Y. 11251

Commanding Officer
NROTC and Naval Administrative Unit
Mass. Inst. of Technology
Cambridge, Mass. 02139

Department of Naval Architecture
and Marine Engineering
Room 5-228
Massachusetts Inst. of Technology
Cambridge, Massachusetts 02139

Commander
Charleston Naval Shipyard
U. S. Naval Base
Charleston, S. C. 29408

Commander
Naval Weapons Center
China Lake, California 93555

Commanding Officer
Office of Naval Research Branch Office
219 South Dearborn St.
Chicago Ill. 60604

Commander
Naval Weapons Laboratory
Attn. Technical Library
Dahlgren Va. 22418

Commander
Naval Weapons Laboratory
Attn: Computation & Analysis Lab.
Dahlgren, Virginia 22448

Commanding Officer
Army Research Office
Attn: ESD - AROD
Box CM, Duke Station
Durham, North Carolina 27706

Commanding Officer
Army Research Office
Box CM, Duke Station
Durham, North Carolina 27706

U.S. Army Mobility Equip. Res. and Dev.
Att: Technical Documents Center
Building 315
Fort Belvoir, Virginia 22060

Commander
Long Beach Naval Shipyard
Long Beach, Calif. 90802

Commanding Officer & Director
Underwater Sound Lab.
Fort Trumbull
Attn: Technical Library
New London, Conn. 06321

Commanding Officer
USN Underwater Weapons and
Research & Engrg Station
Attn: Technical Library
Newport, Rhode Island 02840

Office of Naval Research
New York Area Office
207 W. 24th St.
New York, N. Y. 10011

Director, Naval Research Laboratory (25)
Attn. Library, Code 2029 (ONRL)
Washington, D.C. 20390

Commander
Naval Undersea Research and Dev. Center
3202 East Foothill Blvd.
Pasadena, California 91107

Commanding Officer
Office of Naval Research Branch Office
1030 E. Green St.
Pasadena, Calif. 91101

Commander
Technical Li b. (Code 249b)
Philadelphia Naval Shipyard
Philadelphia, Pa. 19112

Commander
Naval Missile Center
Attn: Technical Library
Point Mugu, Calif. 93041

Commanding Officer & Director
Naval Civil Engineering Lab.
Port Hueneme, Calif. 93041

Commander
Portsmouth Naval Shipyard
Portsmouth New Hampshire 03801

Commander
Norfolk Naval Shipyard
Portsmouth, Virginia 23709

Commander
Naval Command Control Communications
Laboratory Center
San Diego, California 92152

Commander (Code 246P)
Pearl Harbor Naval Shipyard
Box 400
FPO San Francisco 96610

Office of Naval Research
San Francisco Area Office
50 Fell Street
San Francisco, California 94103

Commander
Naval Ordnance Laboratory
Attn: Dr. A. May
White Oak
Silver Spring, Md. 20910

Commander
Naval Ordnance Laboratory
Attn: Dr. A. E. Seigel
White Oak Laboratory
Silver Spring, Md. 20910

Commander
Naval Ordnance Laboratory
Attn: Gas Dynamics Division
White Oak
Silver Spring, Md. 20910

Commander
Naval Ordnance Laboratory
Attn: Librarian
White Oak
Silver Spring, Md. 20910

Commander
Naval Ordnance Laboratory
Attn: Chief, Lib. Div.
White Oak
Silver Spring, Md. 20910

Commanding Officer & Director
Naval Ship Research & Development Center
Washington, D. C. 20007

Commander
Naval Ship Systems Command
Department of the Navy
Attn: Code 6340
Washington, D. C. 20360

Director
U. S. Naval Research Laboratory
Attn: Code 2027 (6)
Washington, D. C. 20390

Chief of Naval Research
Department of the Navy
Attn: Code 438 (3)
Washington, D. C. 20360

Commanding Officer & Director
N. S. R. D. C.
Attn: Code 513
Washington, D. C. 20007

Commander
Naval Ship Systems Command
Attn: Code 6440
Washington, D. C. 20360

Commander
Naval Ship Engr. Center
Concept Design Division
Attn: Code 6420
Washington, D. C. 20360

Commanding Officer & Director
N. S. R. D. C.
Attn: Code 800
Washington, D. C. 20007

Commanding Officer & Director
N. S. R. D. C.
Attn: Code 581
Washington, D. C. 20007

Commanding Officer & Director
N. S. R. D. C.
Attn: Code 550
Washington, D. C. 20007

Commander
Naval Ship Systems Command
Department of the Navy
Attn: Code 6442
Washington, D. C. 20360

Commander
Naval Ship Systems Command
Department of the Navy , Attn: Code 6342A
Washington, D. C. 20360

Commanding Officer & Director
N. S. R. D. C.
Attn: Code 108
Washington, D. C. 20007

Commander Naval Air Systems Command
Department of the Navy
Attn: Code Air 370
Washington, D. C. 20360

Chief of Naval Research
Department of the Navy
Attn: Code 463
Washington, D. C. 20360

Commanding Officer & Director
N. S. R. D. C.
Attn: Code 901
Washington, D. C. 20007

Commanding Officer & Director
N. S. R. D. C.
Attn: Code 940
Washington, D. C. 20007

Commanding Officer & Director
N. S. R. D. C.
Attn: Code 942
Washington, D. C. 20007

Commanding & Director
N. S. R. D. C.
Attn: J. L. Power (589)
Washington, D. C. 20007

Commanding Officer & Director
N. S. R. D. C.
Attn: Code 520
Washington, D. C. 20007

Commander
Naval Ship Systems Command
Department of the Navy
Attn: Code 0341
Washington, D. C. 20360

Commander
Naval Ship Systems Command
Department of the Navy
Attn: Code 6345
Washington, D. C. 20360

Commanding Officer & Director
N. S. R. D. C.
Attn: Code 500
Washington, D. C. 20007

Commander
Naval Ordnance Systems Command
Attn: ORD 03
Washington, D. C. 20360

Commander
Naval Ordnance Systems Command
Attn: ORD 913 (Library)
Washington, D. C. 20360

Commander
Naval Ordnance Systems Command
Attn: ORD 05411
Washington, D. C. 20360

Commander
Naval Ship Systems Command
Department of the Navy
Attn: Code 61500
Washington, D. C. 20360

Commanding Officer and Director
N. S. R. D. C.
Attn: Code 526A
Washington, D. C. 20007

Chief of Naval Research
Department of the Navy
Attn: Code 473
Washington, D. C. 20360

Commanding Officer & Director
N. S. R. D. C.
Attn: Code 521
Washington, D, C. 20007

Commander
Naval Ship Engineering Center
Concept Design Division
Attn: Code 6110
Washington, D, C. 20360

Commander
Naval Ship System Command
Technical Library, Code 2021
Washington, D. C. 20360

Superintendent
Naval Postgraduate School
Attn: Library
Monterey, Calif. 93940

National Academy of Sciences
National Research Council
2101 Constitution Ave., N. W.
Washington, D. C. 20360

Director, Engineering Science Division
National Science Foundation
Washington, D. C. 20550

Director of Research Code RR
National Aeronautics & Space Admin.
600 Independence Ave., S. W.
Washington, D. C. 20546

Division of Engineering
Maritime Administration
441 G. Street, N. W.
Washington, D. C. 20235

Division of Ship Design
Maritime Administration
441 G. Street, N. W.
Washington, D. C. 20235

Commander, R & T Divisions
Air Force Systems Command
Attn: L. M. Medgepeth (APIP- 1)
Wright-Patterson AFB, Ohio 45433

AFOSR (SREM)
1400 Wilson Boulevard
Arlington, Va. 22209

National Science Foundation
Engineering Division
1800 G. Street, N. W.
Washington, D. C. 20550

Defence Research & Dev. Attache
Australian Embassy
1601 Massachusetts Avenue, N.W.
Washington, D.C. 20036

Superintendent
Naval Academy
Attn: Library
Annapolis, Md. 21402

Defense Documentation Ctr.
Cameron Station
Alexandria, Virginia 22314 (20)

Dr. R. E. Wilson
Assoc. Tech. Dir. (Aeroballistics)
Naval Ordnance Laboratory
White Oak
Silver Spring, Md. 20910

Librarian
Department of Naval Architecture
University of California
Berkeley, California 94720

Engineering Library
Plant 25
Grumman Aircraft Engineering Corp.
Bethpage, Long Island, N. Y. 11714

NASA Lewis Research Center
Attn: Library MS 60-3
21000 Brookpark Road
Cleveland, Ohio 44135

Technical Library
Webb Institute of Naval Architecture
Glen Cove, Long Island, N. Y. 11542

Lorenz G. Straub Library
St. Anthony Falls Hydraulic Lab.
Missippi River At 3rd Ave., S. E.
Minneapolis, Minnesota 55414

Engineering Societies Library
345 East 47th Street
New York, N. Y. 10017

NASA, Langley Research Center
Langley Station
Attn: Library MS 185
Hampton, Virginia 23365

National Research Council
Aeronautical Library
Attn: Miss O. M. Leach, Librarian
Montreal Road
Ottawa 7, Canada

Redstone Scientific Information Center
Attn: Chief, Document Section
Army Missile Command
Redstone Arsenal, Alabama 35809

Tech. Library, Code H245C-3
Hunters Point Division
San Francisco Bay Naval Shipyard
San Francisco, California 94135

Fenton Kennedy Document Library E
The Johns Hopkins University
Applied Physics Laboratory
8621 Georgia Ave.
Silver Spring, Maryland 20910

Engineering Library
Dept. 218, Bldg 101
MC Donnel Aircraft Corp.
P.O. Box 516
St. Louis, Missouri 63166

Shipyard Technical Library
Code 246L Bldg. 746
San Francisco Bay Naval Shipyard
Vallejo, California 94592

Library
The Marquardt Corporation
16555 Saticoy
Van Nuys, California 91409

Science & Technology Division
Library of Congress
Washington, D. C. 20540

Librarian Station 5-2
Coast Guard Headquarters
1300 E. Street, N. W.
Washington, D. C. 20226

NASA Scientific & Tech. Info. Fac.
Attn: Acquisitions BR (S-AK/DL)
P.O. Box 33
College Park, Maryland 20740

Library
Aerojet-General Corp.
6352 N. Irwindale Ave.
Azusa, California 91702

The Bunker-Ramo Corporation
Attn: Technical Library
8433 Fallbrook Ave.
Canoga Park, California 91804

Professor L. N. Milne-Thomson
Mathematics Department
University of Arizona
Tucson, Arizona 85721

Professor Finn C. Michelsen
Naval Architecture & Marino Engineering
450 West Engineering Building
University of Michigan
Ann Arbor, Michigan 48106

Dr. E. J. Skudrzyk
Ordnance Research Laboratory
Pennsylvania State University
University Park, Pennsylvania 16801

Dr. C. S. Yih
Department of Engineering Mechanics
University of Michigan
Ann Arbor, Michigan 48108

Professor F. G. Hammitt
University of Michigan
Ann Arbor, Michigan 48108

Professor A. Kuethe
Dept. of Aeronautical Engineering
University of Michigan
Ann Arbor, Michigan 48108

Dr. R. B. Bouch
General Dynamics
Quincy Division
97 E. Howard
Quincy, Mass. 02169

Dr. J. Menkes
Institute for Defense Analyses
400 Army-Navy Drive
Arlington, Virginia 22204

Prof. W. W. Willmarth
Dept. of Aero/space Engineering
University of Michigan
Ann Arbor, Michigan 48104

Professor J. Foa
Dept. of Aeronautical Engineering
Rennsselaer Polytechnic Institute
Troy, New York 12180

Professor R. C. Di Prima
Department of Mathematics
Rennsselaer Polytechnic Institute
Troy, New York 12180

Dr. M. Sevik
Ordnance Research Laboratory
Pennsylvanis State University
University Park, Pa. 16801

Dr. J. M. Robertson
Dept. of Theoretical & Applied Mechanics
University of Illinois
Urbana, Illinois 61803

Professor J. K. Vennard
Dept of Civil Engineering
Stanfo rd Unviersity
Stanford, California 94305

Dr. G. F. Wislicenus
Ordnance Research Laboratory
Pennsylvania State University
University Park, Pennsylvania 16801

Dr. Byrne Perry
Department of Civil Engineering
Stanford University
Stanford, California 94305

Professor E. Y. Hsu
Dept. of Civil Engineering
Stanford University
Stanford, California 94305

Professor D. Gilbarg
Stanford University
Stanford, California 94305

Professor W. R. Sears
126 Honness Lane
Ithaca, New York 14850

Professor F. Zwicky
Department of Physics
California Institute of Technology
Pasadena, California 91109

Professor A. Ellis
University of Calif. San Diego
La Jolla, Calif. 92037

Professor J. M. Killen
St. Anthony Falls Hydraulic Lab.
University of Minnesota
Minneapolis, Minnesota 55414

Professor A. G. Strandhagen
Department of Engineering Mechanics
University of Notre Dame
Notre Dame, Indiana 46556

Professor A. Peters
Institute of Mathematical Sciences
New York University
251 Mercer Street
New York, New York 10003

Professor R. E. Little
University of Michigan Dearborn Campus
4901 Evergreen Road
Dearborn, Michigan 48128

Professor John Laufer
Dept. of Aerospace Engineering
University Park
Los Angeles, California 90007

Dr. Martin H. Bloom
Polytechnic Institute of Brcoklyn
Graduate Center, Dept. of Aerospace
Eng. & Applied Mechanics
Farmingdale, N. Y. 11735

Professor J. J. Foody
Chairman, Engineering Department
State University of New York
Maritime College
Bronx, New York 10465

Professor John Miles
% I. G. P. P.
University of Calif. San Diego
La Jolla, Calif. 92038

Professor T. Y. Wu
California Insitute of Technology
Pasadena, California 91109

Mr. C. S. Song
St. Anthony Falls Hydraulic Lab.
University of Minnesota
Minneapolis, Minnesota 55414

Professor M. A. Abkowitz
Dept. of Naval Architecture and
Marine Engineering
Massachusetts Inst. of Technology
Cambridge, Massachusetts 02139

Professor M. S. Uberoi
Department of Aeronautical Engineering
University of Colorado
Boulder, Colorado 80303

Professor G. L. Von Eschen
Dept. of Aeronautical Astronautical Engrg.
Ohio State University
Columbus, Ohio 43210

Professor R. F. Probstein
Department of Mechanical Engineering
Massachusetts Inst. of Technology
Cambridge, Massachusetts 02139

Professor A. T. Ippen
Massachusetts Inst. of Technology
Cambridge, Massachusetts 02139

College of Engineering
Office of Research Services, Univ. of Calif.
Berkeley, California 94720

Professor M. Holt
Division of Aeronautical Sciences
University of California
Berkeley, California 94720

Prof. J. V. Wehausen
Department of Naval Architecture
University of California
Berkeley, California 94720

Professor G. Birkhoff
Harvard University
Cambridge, Massachusetts 02138

Dr. E. E. Sechler
Executive Officer for Aero.
California Institute of Technology
Pasadena, California 91109

Professor A. Acosta
California Institute of Technology
Pasadena, California 91109

Dr. Irving C. Statler, Head
Applied Mechanics Department
Cornell Aeronautical Lab. Inc.
P. O. Box 235
Buffalo, N. Y. 14204

School of Applied Mathematics
Indiana University
Bloomington, Indiana 47401

Mr. J. M. Wetzel
St. Anthony Falls Hydraulic Lab.
University of Minnesota
Minneapolis, Minnesota 55414

Professor J. Ripkin
St. Anthony Falls Hydraulic Lab.
University of Minnesota
Minneapolis, Minnesota 55414

Professor M. V. Morkvin
Dept. of Mech. and Aerospace Eng.
Illinois Institute of Technology
Chicago, Illinois 60616

Director
Scripps Institution of Oceanography
University of California
La Jolla, California 92037

Professor A. F. Charwat
Department of Engineering
University of California
Los Angeles, California 90024

C. E. Bowers (2)
St. Anthony Falls Hydraulic Lab.
University of Minnesota
Minneapolis, Minnesota 55414

Professor A. Charnes
The Technological Institute
Northwestern University
Evanston, Illinois 60201

Dr. O. Grim
Institute fur Schiffbau
Lammersieth 90
2, Hamburg 33, Germany

Dr. S. F. Hoerner
148 Busteed Drive
Midland Park, New Jersey 07432

Mr. D. Savitsky
Stevens Institute of Technology
Davidson Laboratory
Hoboken, New Jersey 07030

Mr. J. P. Breslin
Stevens Institute of Technology
Davidson Laboratory
Hoboken, New Jersey 07030

Dr. John E. Mayer, Jr.
Research & Engineering Center
Ford Motor Company
P. O. Box 2053
Dearborn, Michigan 48123

Professor Frederick G. Hammitt
Dept. of Mech. Eng. The Univ. of Mich.
College of Engineering
Ann Arbor, Michigan 48104

J. D. Malloy, President
Hydrosystems, Inc.
19 Engineers Lane
Farmingdale, New York 11735

Mr. J. Z. Lichtman, Code 937
Naval Applied Science Lab.
Brooklyn, New Yo rk 11251

Dr. Ronald Smelt
Vice President & Chief Scientist
Lockheed Aircraft Corporation
Burbank, California 91503

Dr. H. Reichardt, Director
Max Planck Institut fur Stromungsforschung
Bottingerstrasse 6-8
Gottingen, Germany

Dr. H. W. Lerbs
Hamburgische Schiffbauversuchsanstalt
Bramfelder Strasse 164
Hamburg 33, Germany

Dr. H. Schwaneche
Hamburgische Schiffbauversuchsanstalt
Bramfelder Strasse 164
Hamburg 33, Germany

DIPL. Ing. A Gross
Versuchsanstalt fur Wasserbau & Schiffbau
Schleuseninsel IM Tiergarten
Berlin, Germany

Professor Dr.-Ing. S. Schuster
Versuchsanstalt fur Wasserbau & Schiffbau
Berlin, Germany

Dr. K. Eggers
Instiut fur Schiffbau
University of Hamburg
Laemmersieth 90
2 Hamburg 33, Germany

Prof. Dr. Ir. J.D. Van Manen
Netherlands Ship Model Basin
Haagsteeg 2, Postbox 28
Wageningen, The Netherlands

Professor S. Siestrunck
Bureau D'Analyse de Recherches
Appliquees
6 Rice Louis Pasteur
92 Boulogne, France

The Principel
College of Engineering
Guindy, Madras-25
India

Ir. W. Spuyman
Netherlands Ship Research Centre TNO
Leeghwaterstraat 5
Postbus 29, Delft, Netherlands

Prof. Ir. J. Gerritsma
Head Shipbuilding Lab., Tech. Univ.
Mekelweg 2
Delft, The Netherlands

Professor Carl Prohaska
Hydro-og Aerodynamisk Laboratorium
Lyngby, Denmark

Mr. Alfonso Alcedan L., Director
Laboratorio Nacional de Hydraulics
Antiguo Cameno A. Ancon
Casilla Jostal 682
Lima, Peru

Professor J. K. Lunde
Skipmodelltanken
Trondheim, Norway

Dr. K. Taniguchi
Mitsublishi Shipbuilding & Eng. Co.
Nagasaki, Japan

Research Committee in Information
The American Society of Mechanical Engs.
345 East 47th Street
New York, New York 10017 (2)

Society of Naval Architects and
Marine Engineers
74 Trinity Place
New York, New York 10006

Convair Division of General Dynamics
P.O. Box 12009
Attn: Library (128-00)
San Diego, Calif. 92112

Editor
Applied Mechanics Review
Southwest Research Institute
8500 Culebra Road
San Antonio, Texas 78206

The Western Company
Research Division
2201 North Waterview Parkway
Richardson, Texas 75080

Chrysler Corporation
MGR. Advance Projects Organ.
P.O. Box 1827
Detroit, Michigan 48231

Director
Hudson Laboratories
Dobbs Ferry, New York 10522

Ocean Systems
North American Aviation, Inc.
12214 Lakewood Blvd.
Downey, California 90241

Mr. Eugene F. Baird
Chief of Dynamic Analysis
Grumman Aircraft Eng. Corp.
Bethpage, Long Island, N.Y. 11714

Dr. B. Sternlicht
Mechanical Technology Incorporated
968 Albany-Shaker Road
Latham, New York 12110

Mr. P. Eisenberg, President
Hydronautics, Inc.
Pindell School Rd.
Howard Conuty
Laurel, Md. 20810

Dr. Jack Kotik
TRG. Incorporated
Route 110
Melville, New York 11746

Mr. R. E. MacPherson
Oak Ridge National Laboratory
P.O. Box Y
Oak Ridge, Tennessee 37831

Dr. F. R. Hama
Gas Dynamics Lab.
Princeton University
Princeton, N. J. 08540

Southwest Research Institute
San Antonio, Texas 78212

Dr. H. N. Abramson
Southwest Research Institute
8500 Culebra Road
San Antonio, Texas 78228

Mr. Warren Bloomfield
Manager, Systems Engineering
Lycoming Division Avco Corporation
Stratford, Connecticut 06497

Dr. F. W. Boggs
U. S. Rubber Company
Research Center
Wayne, New Jersey 07470

Mr. A. Silverleaf
National Physical Laboratory
Teddington, Middlesex, England

Mr. R. W. Kermeen
Lockheed Missiles & Space Company
Department 57101 Bldg. 150
Sunnyvale, California 94086

Otto Decker, Manager
Friction & Lubrication Lab.
Franklin Institute
20th & Parkway
Philadelphia, Penna 19103

Dr. Paul Kaplan
Oceanics, Inc.
Plainview, Long Island, N. Y. 11803

Mr. Ross Hatte, Chief
Marine Performance Staff
The Boeing Co., Aero-Space Division
P. O. Box 3707
Seattle, Washington 98124

Dr. A. Powell
Code 900
N.S.R.D.
Washington, D. C. 20007

Mr. H. Stern
Manager, Fluids Branch
General Electric Company
P.O. Box 8
Schenectady, New York 12301

Mr. Schuyler Kleinhans
Vice President - Engineering
Douglas Aircraft Company, Inc.
Santa Monica, California 90406

Professor J. William Holl
Professor of Aerospace Engineering
Ordnance Research Laboratory
University Park, Pa. 16801

W. B. Barkley
General Dynamics Corp.
Electric Boat Division
Marine Tech. Center
P.O. Box 911
San Diego, California 92112

Commanding Officer
Attn: Tech. Lib. (Bldg) 313
Aberdeen Proving Ground, Md. 21005

Commander
Portsmouth Naval Shipyard
Portsmouth, New Hampshire 03801

Unclassified
Security Classification

DOCUMENT CONTROL DATA - R & D

(Security classification of title, body of abstract and indexing annotation must be entered when the overall report is classified)

1. ORIGINATING ACTIVITY (Corporate author)	2a. REPORT SECURITY CLASSIFICATION
California Institute of Technology Division of Engineering and Applied Science	Unclassified
	2b. GROUP Not applicable

3. REPORT TITLE

COLLAPSE OF AN INITIALLY SPHERICAL CAVITY IN THE NEIGHBORHHOD OF A SOLID BOUNDARY

4. DESCRIPTIVE NOTES (Type of report and inclusive dates)

Technical Report

5. AUTHOR(S) (First name, middle initial, last name)

Plesset, Milton S.
Chapman, Richard B.

6. REPORT DATE	7a. TOTAL NO. OF PAGES	7b. NO. OF REFS
June 1970	22	11

8a. CONTRACT OR GRANT NO.	9a. ORIGINATOR'S REPORT NUMBER(S)
N00014-67-0094-0009 b. PROJECT NO.	Report No. 85-49
c.	9b. OTHER REPORT NO(S) (Any other numbers that may be assigned this report)
d.	

10. DISTRIBUTION STATEMENT

This document has been approved for public release and sale; its distribution is unlimited.

11. SUPPLEMENTARY NOTES	12. SPONSORING MILITARY ACTIVITY
	Office of Naval Research

13. ABSTRACT

Vapor bubble collapse problems lacking spherical symmetry are solved here using a numerical method designed especially for these problems. Viscosity and compressibility in the liquid are neglected. The method uses finite time steps and features an iterative technique for applying the boundary conditions at infinity directly to the liquid at a finite distance from the free surface. Two specific cases of initially spherical bubbles collapsing near a plane solid wall were simulated: a bubble initially in contact with the wall, and a bubble initially half its radius from the wall at the closest point. It is shown that the bubble develops a jet directed towards the wall rather early in the collapse history. Free surface shapes and velocities are presented at various stages in the collapse. Velocities are scaled like $(\Delta p/\rho)^{\frac{1}{2}}$ where ρ is the density of the liquid and Δp is the constant difference between the ambient liquid pressure and the pressure in the cavity. For

$$\frac{\Delta p}{\rho} = 10^6 \left(\frac{\text{cm}}{\text{sec}}\right)^2 \approx \frac{\text{1 atm.}}{\text{density of water}}$$

the jet had a speed of about 130 m/sec in the first case and 170 m/sec in the second when it struck the opposite side of the bubble. Such jet velocities are of a magnitude which can explain cavitation damage. The jet develops so early in the bubble collapse history that compressibility effects in the liquid and the vapor are not important.

DD FORM 1 NOV 65 1473 (PAGE 1)

S/N 0101-807-6801

Unclassified
Security Classification

14. KEY WORDS	LINK A		LINK B		LINK C	
	ROLE	WT	ROLE	WT	ROLE	WT
Cavitation Cavity collapse						